

CHEMISTRY

A European Journal

A Journal of



Accepted Article

Title: A Di-ruthenium Complex of a N-Pyridyl-o-Aminophenol Derivative: A Route to Mixed Valency

Authors: Prasanta Ghosh, Debarpan Dutta, and Suman Kundu

This manuscript has been accepted after peer review and appears as an Accepted Article online prior to editing, proofing, and formal publication of the final Version of Record (VoR). This work is currently citable by using the Digital Object Identifier (DOI) given below. The VoR will be published online in Early View as soon as possible and may be different to this Accepted Article as a result of editing. Readers should obtain the VoR from the journal website shown below when it is published to ensure accuracy of information. The authors are responsible for the content of this Accepted Article.

To be cited as: *Chem. Eur. J.* 10.1002/chem.201903028

Link to VoR: <http://dx.doi.org/10.1002/chem.201903028>

Supported by
ACES

WILEY-VCH

A Di-ruthenium Complex of a N-Pyridyl-*o*-Aminophenol Derivative: A Route to Mixed Valency

Debarpan Dutta,^[a] Suman Kundu^[a] and Prasanta Ghosh^{*[a]}

Abstract: A *N*-pyridyl-*o*-aminophenol derivative that stabilizes mixed-valence states of ruthenium ion is disclosed. A diruthenium complex, $[(L_{IQ}^0)Ru_2Cl_5] \cdot MeOH$ (**1**·MeOH) was successfully isolated, where L_{IQ}^0 is the *o*-iminobenzoquinone form of 2-((3-nitropyridin-2-yl)amino)phenol ($L_{AP}H_2$). In **1**, L_{IQ}^0 towards one ruthenium centre is a NO-donor redox noninnocent, while towards another ruthenium it is a pyridine donor redox innocent ligand. **1** is a diruthenium (II, III) mixed valence complex, $[Ru^{II}(L_{IQ}^0)(\mu-Cl)_2Ru^{III}]$, with a minor contribution of diruthenium (III, III) state, $[Ru^{III}(L_{ISQ}^{\bullet-})(\mu-Cl)_2Ru^{III}]$ where $L_{ISQ}^{\bullet-}$ is the *o*-iminobenzosemiquinonate anion radical form of the ligand. **1**⁻ and **1**⁺ are respectively diruthenium (II, II), $[Ru^{II}(L_{IQ}^0)(\mu-Cl)_2Ru^{II}]$, and diruthenium (III, III), $[Ru^{III}(L_{IQ}^0)(\mu-Cl)_2Ru^{III}]$, complexes of L_{IQ}^0 . **1**²⁻ is a diruthenium (II, II) complex of *o*-iminobenzosemiquinonate anion radical ($L_{ISQ}^{\bullet-}$), $[Ru^{II}(L_{ISQ}^{\bullet-})(\mu-Cl)_2Ru^{II}]$ with a minor contribution of diruthenium (III, II) form, $[Ru^{III}(L_{AP}^{2-})(\mu-Cl)_2Ru^{II}]$. **1**²⁺ is a diruthenium (III, IV) mixed valence complex of L_{IQ}^0 , $[Ru^{III}(L_{IQ}^0)(\mu-Cl)_2Ru^{IV}]$. **1** and **1**²⁺ exhibit inter valence charge transfer transitions at 1300 and 1370 nm.

Introduction

Bimetallic complex ion with Robin-Day Class-II and III states are significant in analyzing the electron transfer reactions, inter valence charge transfer (IVCT) transitions, electrically conducting and magnetic properties.¹ To expand this area, ligand based mixed-valency has also been investigated sincerely in several aspects.² The mixed valence molecular systems are equally important in material and chemical science as well as metallo-protein chemistry.³ In this regard, the first mixed valence ion, $[(NH_3)_5Ru(pz)Ru(NH_3)_5]^{5+}$, where *pz* is a bridging pyrazine ligand, reported by Creutz and Taube was considered as the path-maker of this research area.⁴ In this complex ion, the sum of the oxidation numbers of two metal ions is an odd integer.

It is a calculated value based on the oxidation number of the individual metal ions, as all the bridging and terminal co-ligands of two ruthenium ions are redox innocent. However, introduction of a redox non-innocent ligand to this unit will make a difference and produce a bimetallic unit that involves a difference of oxidation numbers of two metal ions of even less than unity. Being emboldened by this idea, we envisage that the Type B and C molecules as listed in Chart 1 are significant to be modelled, where L_I is a redox innocent ligand and L_{NI} is a redox noninnocent ligand.

As the redox non innocence of the *pz* ligand was not established so far, the Creutz and Taube ion has been defined here as a Type A complex ion. Kaim and Lahiri reported several Types of B complexes containing redox active bridging ligands.⁵ Lahiri reported a mixed valence Type B complex, where L_{NI} is unsymmetrical.⁵ⁱ

$[(L_I)Ru-(L_I)-Ru(L_I)]^{n+}$	Type A
$[(L_I)Ru-(L_{NI})-Ru(L_I)]^{n+}$	Type B
$[(L_{NI})Ru-(L_I)-Ru(L_I)]^{n+}$	Type C

Chart 1. Three types of diruthenium complexes containing redox innocent (L_I) and redox noninnocent (L_{NI}) ligands.

However, no Type C complex was documented so far. The electronic environments of the two metal ions in Type C complexes are not similar and elucidation of the electronic states of the members of the redox series of the unsymmetrical Ru_2 -core is a worthy investigation. Location of the electron transfer centre in this multi-redox active unit and justification of it will expand the knowledge that is momentous in exploring the metal to metal electron transfer reaction.

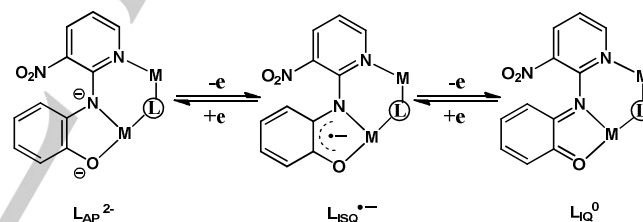
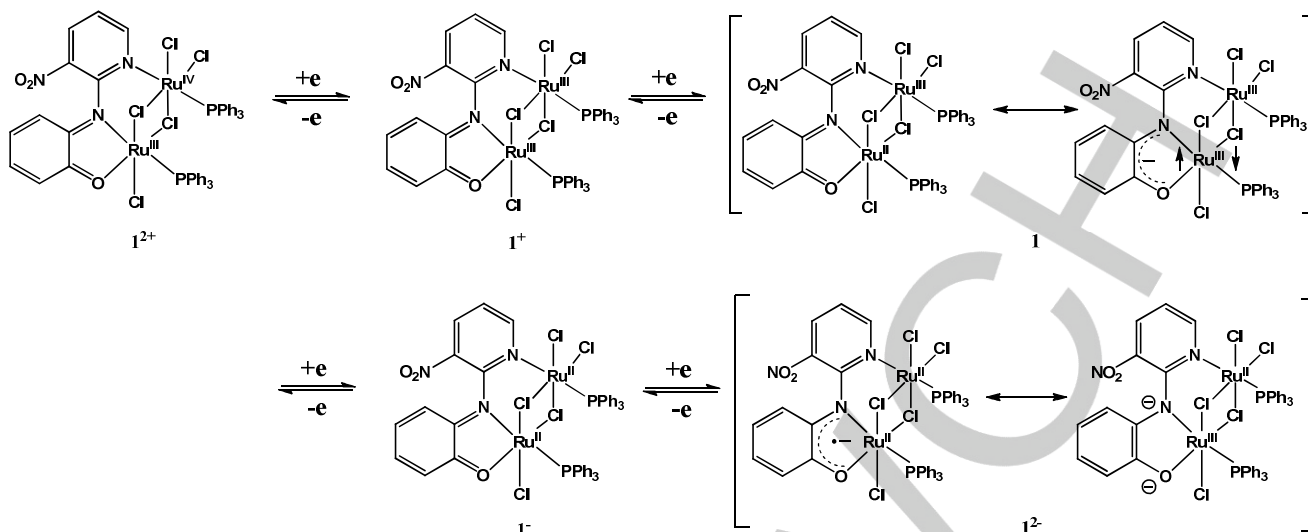


Chart 2. Three redox states of $L_{AP}H_2$, where L is a bridging ligand.

In this effort, we have been successful to synthesize a *N*-pyridyl-*o*-aminophenol derivative, 2-((3-nitropyridin-2-yl)amino)phenol ($L_{AP}H_2$) that can bridge producing Type C complexes of transition metal ions as depicted in Chart 2. A diruthenium complex of the type $[(L_{IQ}^0)Ru_2Cl_5(PPh_3)_2]$ (**1**) was successfully isolated, where L_{IQ}^0 is the *o*-iminobenzoquinone form of $L_{AP}H_2$. In **1**, L_{NI} is the aminophenol compartment, L_I are the two ($\mu-Cl$) and the pyridine compartment of the of $L_{AP}H_2$ ligand. The deprotonated $L_{AP}H_2$ exhibits three distinct redox states as the dianionic *o*-amidophenolate (L_{AP}^{2-}), *o*-iminobenzosemiquinonate anion radical ($L_{ISQ}^{\bullet-}$) and L_{IQ}^0 as shown in Chart 2.⁶ In **1**, the redox state of $L_{AP}H_2$ is L_{IQ}^0 with a minor contribution of $L_{ISQ}^{\bullet-}$ and **1** is defined as a mixed valence diruthenium (II, III) complex of type $[(PPh_3)(Cl)_2Ru^{II}(L_{IQ}^0)(\mu-Cl)_2Ru^{III}(Cl)(PPh_3)]$ with a minor contribution of $[(PPh_3)(Cl)_2Ru^{III}(L_{ISQ}^{\bullet-})(\mu-Cl)_2Ru^{III}(Cl)(PPh_3)]$ as depicted in Scheme 1.

[a] Department of Chemistry
R. K. Mission Residential College, Narendrapur
Kolkata 700103, West Bengal, India
E-mail: ghosh@pghosh.in

Supporting Information: Crystallographic data of **1**·MeOH, ESI mass and ¹H NMR spectra of $L_{AP}H_2$, ESI mass spectra of **1** (positive and negative), EPR spectra and gas phase and solution optimized coordinates.



Scheme 1. Diruthenium (III, IV), diruthenium (III, III), diruthenium (II, III), diruthenium (II, II) states containing the L_{IO}^0 form and a diruthenium (II, II) state containing the L_{ISO}^* form.

The redox behavior of **1** in which two ruthenium centres are not equivalent, has been investigated by cyclic voltammetry. **1** is electrochemically active and undergoes successive two separate, reversible one-electron reductions due to formation of diruthenium (II, II) complexes of types $[(PPh_3)(Cl)Ru^{II}(L_{IO}^0)(\mu-Cl)_2Ru^{II}(Cl)_2(PPh_3)]^-$ (**1**) and $[(PPh_3)(Cl)Ru^{II}(L_{ISO}^*)(\mu-Cl)_2Ru^{II}(Cl)_2(PPh_3)]^{2-}$ (**1**⁻). One electron oxidation of **1** generates a diruthenium (III, III) complex of the type $[(PPh_3)(Cl)Ru^{III}(L_{IO}^0)(\mu-Cl)_2Ru^{III}(Cl)_2(PPh_3)]^+$ (**1**⁺) and further oxidation affords a diruthenium mixed valence (III, IV) complex, $[(PPh_3)(Cl)Ru^{III}(L_{IO}^0)(\mu-Cl)_2Ru^{IV}(Cl)_2(PPh_3)]^{2+}$ (**1**²⁺) as summarized in Scheme 1. **1**⁻, **1**²⁻, **1**⁺ and **1**²⁺ were not isolated, but these were generated by constant potential bulk electrolysis experiments. The molecular and electronic structures of **1** and the related species were confirmed by single crystal X-ray crystallography, EPR spectroscopy, spectroelectrochemical measurements, inter valence charge transfer (IVCT) transitions and broken symmetry (BS) density functional theory (DFT) calculations.

Experimental Section

Materials and Physical Measurements. Reagents or analytical grade materials were obtained from *Sigma-Aldrich* and used without further purification. Spectroscopic grade solvents were used for spectroscopic and electrochemical measurements. The C, H and N contents of the compounds were obtained from a Perkin-Elmer 2400 Series II elemental analyzer. Infrared spectra of the samples were measured from 4000 to 400 cm^{-1} with KBr pellets at room temperature on a Perkin-Elmer Spectrum RX 1 FT-IR spectrophotometer. ¹H NMR spectra were obtained at 295 K on a Bruker DPX 500 MHz spectrometer. ESI mass spectra were recorded on a micro mass Q-TOF mass spectrometer. Electronic absorption spectra were recorded on a Perkin-Elmer

Lambda 750 spectrophotometer of range 3300-190 nm. Magnetic susceptibilities at 298 K were measured on a Sherwood Magnetic Susceptibility Balance. The X-band EPR spectra were measured on a Magnettech GmbH MiniScope MS400 spectrometer (equipped with temperature controller TC H03), where the microwave frequency was measured with an FC400 frequency counter. The EPR spectra were simulated using Easy Spin software. The electro analytical instrument, BASi Epsilon-EC for cyclic voltammetric experiments in CH_2Cl_2 solutions containing 0.2 M tetrabutylammonium hexafluorophosphate as a supporting electrolyte was used. The BASi platinum working electrode, platinum auxiliary electrode, Ag/AgCl reference electrode were used for the electrochemical measurements. The redox potential data reported were referenced to ferrocenium/ferrocene, Fc^+/Fc , couple. 0.5 mm SEC-C thin layer quartz glass spectroelectrochemical cell kit with platinum gauze working electrode (light path length of 1 mm) was used for spectroelectrochemistry measurements.

Syntheses. 2-((3-Nitropyridin-2-yl)amino)phenol ($L_{AP}H_2$). To 2-chloro-3-nitropyridine (316 mg, 2.0 mmol) in *N,N*-dimethylformamide (3 mL) in a 100 ml round-bottom flask were added 2-aminophenol (218 mg, 2.0 mmol) followed by a pinch of potassium carbonate (~300 mg). The reaction mixture was refluxed at 363-365 K on an oil bath for 3 h. The reaction mixture was cooled at room temperature and the reddish slurry was poured into 200 ml ice-cold water in a beaker and stirred for 30 min. A reddish compound separated out, which was filtered through a suction pump and the residue obtained was dried under air. The collected mass was purified by column chromatography using basic alumina and dichloromethane as an eluent. The red product was finally re-crystallised from a methanol solution. Yield: 322 mg. (70% with respect to 2-aminophenol). Mass spectral data [electrospray ionization (ESI), positive ion, CH_2Cl_2]: m/z 231.08 for $[L_{AP}H_2]^+$. Anal. Calcd for

$C_{11}H_9N_3O_3$: C, 57.14; H, 3.92; N, 18.17. Found: C, 56.79; H, 3.78; N, 18.06. 1H NMR ($CDCl_3$, 500 MHz, 298 K): δ 8.63 (d, 1H, $J = 4.5$ Hz), δ 8.53 (d, 1H, $J = 8.0$ Hz), δ 8.44 (d, 1H, $J = 4.0$ Hz), δ 8.22 (d, 1H, $J = 8.0$ Hz), δ 7.46 (t, 1H, $J = 6.5$ Hz), δ 7.35 (d, 1H, $J = 8.0$ Hz), δ 7.14 (t, 1H, $J = 7.5$ Hz), δ 6.86 (t, 1H, $J = 8.0$ Hz), δ 6.79 (dd, 1H, $J = 8.5$; 4.5 Hz). IR/ cm^{-1} (KBr): ν 3494 (m), 3313 (s), 3049 (s), 1611 (m), 1583 (s), 1538 (s), 1517 (s), 1459 (s), 1416 (m), 1354 (s), 1330 (m), 1277 (m), 1239 (m), 1191 (m), 1159 (m), 859 (m), 745 (m).

$[(L_{AQ})Ru_2Cl_5] \cdot MeOH$ (1**·MeOH).** To $L_{AP}H_2$ (23 mg, 0.10 mmol) in toluene (25 mL) in a round bottom flask was added $[Ru^{II}(PPh_3)_3Cl_2]$ (190 mg, 0.20 mmol) and the mixture was stirred for 3h in air at 298 K. A reddish solution was obtained and it was allowed to evaporate slowly in air at room temperature. After 5–7 days, a dark-violet residue separated out, which was collected upon filtration and dried. Diffusion of *n*-hexane to a CH_2Cl_2 solution of the residue containing a few drops of MeOH in air afforded purple needles of **1**·MeOH, which are collected upon filtration and dried in air. Yield: 52 mg. (46% with respect to $L_{AP}H_2$). Single crystals for X-ray diffraction analysis were collected from this crop. Elemental analyses were performed after evaporating the solvent of crystallization under high vacuum. Mass spectral data [electrospray ionization (ESI), positive ion, CH_2Cl_2]: m/z 579 for $[(L_{AQ})Ru_2Cl_5(CH_3CN)]^+$, 492 $[(L_{AP}H_2)PPh_3]$ and 333 $[(L_{AQ}H)Ru]^+$; [electrospray ionization (ESI), negative ion, CH_2Cl_2]: m/z 609 for $[(L_{AQ})Ru_2Cl_5]$, 490 $[(L_{AP}H)PPh_3]$. Anal. Calcd for $C_{47}H_{37}Cl_5N_3O_3P_2Ru_2$ (FW, 1133.16): C, 49.82; H, 3.29; N, 3.71. Found: C, 49.68; H, 3.14; N, 3.57. IR/ cm^{-1} (KBr): ν 3433 (broad), 3055 (s), 2923 (s), 2852 (m), 1631 (s), 1591 (s), 1536 (s), 1437 (s), 1180 (m), 1117 (s), 1090 (m), 746 (s), 722 (s), 693 (s), 542 (s).

Single Crystal X-ray Structure Determination. A single crystal of **1**·MeOH (CCDC No. 1890212) was picked up with a nylon loop and was mounted on a Bruker APEX-II CCD and Bruker AXS D8 QUEST ECO diffractometer equipped with a Mo-target rotating-anode X-ray source and a graphite monochromator (Mo-K α , $\lambda = 0.71073$ Å). Final cell constants were obtained from least-squares fits of all measured reflections. Intensity data were corrected for absorption using intensities of redundant reflections. The structures were readily solved by direct methods and subsequent difference Fourier techniques. The crystallographic data of **1** have been listed in Table S1. The SHELXS-97 (Sheldrick 2008) software package was used for solution and SHELXL-2014/6 (Sheldrick, 2014) was used for the refinement.⁷ All non-hydrogen atoms were refined anisotropically. Hydrogen atoms were placed at the calculated positions and refined as riding atoms with isotropic displacement parameters.

Broken Symmetry (BS) Density Functional Theory (DFT) Calculations. All DFT calculations were performed with the ORCA program package.⁸ All calculations were done by the hybrid PBE0 DFT method.⁹ The gas phase geometry of **1** was optimized with a doublet spin state and the gas phase geometries of **1**⁻ and **1**⁺ were optimized with the singlet spin

state, and those of **1**²⁺ and **1**²⁻ were done with the doublet spin state. Similarly the geometries of **1**, **1**⁺ and **1**⁻ were optimized in CH_2Cl_2 using CPCM model. The BS calculations were performed for **1**⁺ and **1**²⁺ ions. Thus, the gas phase geometries of the **1**⁺ and **1**²⁺ ions were also optimized with triplet and quartet spin states. The BS $M_S = 0$ state of **1**⁺ was calculated by BS (1,1) formalism, while the BS $M_S = 1/2$ state of **1**²⁺ was calculated by ORCA flip spin DFT method.¹⁰ For all calculations, the all-electron valence double-zeta, def2-SVP,¹¹ basis set with “new” polarisation function developed by Karlsruhe group was used for P, N, Cl, O, C and H atoms. For Ru atom def2-TZVP,¹¹ a valence triple-zeta basis set with new polarisation function was used. Resolution of Identity RIJCOSX^{12a} approximation with def2/J auxiliary basis set for Coulomb and HF exchange integral for HF and hybrid DFT methods were employed for self-consistent field (SCF) gradient calculations.^{12b} The geometry optimizations were carried out in redundant internal coordinates without imposing symmetry constraints. The SCF calculations were converged tightly (1×10^{-8} Eh in energy, 1×10^{-7} Eh in the density change and 1×10^{-7} in maximum element of the DIIS error vector). Time-dependent (TD) DFT^{13a-c} calculation for electronic absorption spectra was carried out on **1** using B3LYP functional in CH_2Cl_2 with the application of the CPCM model^{13d-e} to screen the effects of solvent.

Results and Discussion

Syntheses and Characterization. Details of the syntheses of $L_{AP}H_2$ and **1** and their characterization data are outlined in the experimental section. $L_{AP}H_2$ was isolated in good yield from a single step reaction of 2-chloro-3-nitropyridine and 2-aminophenol (1:1) in *N,N*-dimethylformamide at 363–365 K. Reaction of $L_{AP}H_2$ with $[Ru^{II}(PPh_3)_3Cl_2]$ in toluene at 298 K affords a brownish solution, that on evaporation in air produces a purple crystalline solid of **1**. **1** is paramagnetic with one unpaired spin, $\mu_{eff} = 1.81$ BM at 298 K. Diffusion of *n*-hexane into a dichloromethane-methanol (10:1) solution of **1** in air produces single crystals of **1**·MeOH in good yield. The ESI mass and 1H NMR spectra of $L_{AP}H_2$ are illustrated in Figures S1 and S2 (Supporting information). The ESI mass spectrometry affirms that the $[Ru(\mu-Cl)_2Ru]$ moiety in **1** is stable in solution and the m/z peaks due to the dinuclear core were detected both in ESI positive and negative spectra as shown in Figures S3 and S4. However the analysis infers that the coordinated PPh_3 ligands are labile and undergo dissociation in solution. The molecular geometry of **1**·MeOH in the crystal was confirmed by single crystal X-ray crystallography and the redox activity was investigated by cyclic voltammetry (*vide infra*).

X-ray Crystallography. **1**·MeOH crystallizes in the *P*-1 space group. The molecular geometry of **1**·MeOH in crystals with the atom-labelling scheme is illustrated in Figure 1. The significant bond parameters are listed in Table 1. In **1**, L_{AQ}^0 acts as a bridging ligand and towards $Ru(1)$ L_{AQ}^0 is a redox non-innocent

Table 1. Selected Experimental Bond Lengths [Å] of **1**•MeOH and the Corresponding Calculated Bond Lengths of **1** and **1**²⁺ with Doublet Spin State, **1**¹ with Singlet Spin State, **1**¹ with Singlet and Broken Symmetry (BS) M_S = 0 and **1**²⁺ with Doublet and BS (2,1) M_S = ½ Spin States

Bond	experimental	calculated						
		1		1 ¹		1 ²⁺		BS (2,1) (M _S = ½)
		(M _S = ½)	(M _S = 0)	(M _S = ½)	M _S = 0	BS (1,1) (M _S = 0)	M _S = ½	
Ru(1)-P(1)	2.328(2)	2.309	2.304	2.279	2.322	2.375	2.367	2.367
Ru(1)-O(1)	1.994(3)	1.991	1.987	1.996	1.976	2.015	2.005	2.004
Ru(1)-N(1)	1.994(3)	2.034	1.990	2.046	1.986	2.019	2.030	2.030
Ru(1)-Cl(1)	2.347(2)	2.333	2.387	2.415	2.316	2.266	2.249	2.252
Ru(1)-Cl(2)	2.326(2)	2.384	2.382	2.411	2.374	2.326	2.346	2.350
Ru(1)-Cl(3)	2.497(2)	2.534	2.460	2.496	2.559	2.517	2.651	2.667
Ru(2)-Cl(2)	2.308(2)	2.440	2.399	2.407	2.361	2.447	2.357	2.474
Ru(2)-Cl(3)	2.418(2)	2.441	2.489	2.520	2.459	2.472	2.480	2.358
Ru(2)-Cl(4)	2.311(2)	2.313	2.389	2.424	2.243	2.286	2.236	2.255
Ru(2)-Cl(5)	2.329(2)	2.322	2.393	2.425	2.245	2.302	2.237	2.240
Ru(2)-P(2)	2.316(2)	2.334	2.295	2.255	2.377	2.343	2.408	2.423
Ru(2)-N(2)	2.289(3)	2.238	2.189	2.201	2.261	2.239	2.315	2.323
C(1)-O(1)	1.276(6)	1.283	1.286	1.307	1.277	1.265	1.265	1.264
C(1)-C(2)	1.429(7)	1.416	1.415	1.406	1.420	1.424	1.423	1.423
C(2)-C(3)	1.340(10)	1.375	1.378	1.392	1.371	1.367	1.366	2.366
C(3)-C(4)	1.423(11)	1.421	1.416	1.399	1.427	1.436	1.439	1.439
C(4)-C(5)	1.352(8)	1.374	1.379	1.393	1.372	1.367	1.368	1.367
C(5)-C(6)	1.429(7)	1.417	1.415	1.403	1.419	1.425	1.424	1.424
C(6)-C(1)	1.435(7)	1.444	1.439	1.425	1.450	1.459	1.465	1.465
C(6)-N(1)	1.357(6)	1.350	1.359	1.385	1.348	1.332	1.333	1.333
N(1)-C(7)	1.412(5)	1.387	1.385	1.355	1.397	1.409	1.407	1.408

N,O-chelating ligand,⁶ while towards Ru(2) it is a redox innocent monodentate pyridine nitrogen donor ligand. Ru(2) binds two terminal Cl ligands, while Ru(1) contains only one terminal Cl ligand. Thus the distorted RuONPCl₃ and RuNPCl₄ octahedrons are not equivalent. Notably the bond lengths of the two coordination spheres are significantly different. All the Ru(2)-Cl terminal bond lengths are relatively shorter than the corresponding Ru(1)-Cl lengths. The Ru(1)-Cl(1) bond length is 2.347(2) Å, while the Ru(2)-Cl(4) and Ru(2)-Cl(5) bond lengths are 2.311(2) and 2.329(2) Å that are consistent with a ruthenium (III) state. For comparison, the terminal and bridging Ru-Cl bond lengths of diruthenium (III, III), diruthenium (II, II), diruthenium (II, III) and **1**•MeOH are listed in Chart 3.¹⁴⁻¹⁶ The average Ru-Cl_b (b = bridging) bond lengths are significantly different for [Ru^{III}(μ-Cl)₃Ru^{III}], [Ru^{II}(μ-Cl)₃Ru^{III}] and [Ru^{II}(μ-Cl)₃Ru^{II}] units. The calculated average Ru-Cl_b lengths for them respectively are 2.429(2), 2.446(2) and 2.485 Å. **1**•MeOH contains a [Ru(μ-

Cl)₂Ru] unit and notably, the bridging Ru(2)-Cl(2) and Ru(2)-Cl(3) bond lengths in **1**•MeOH, 2.308(2) and 2.418(2) Å are relatively shorter than Ru(1)-Cl(2) and Ru(1)-Cl(3) bond lengths, 2.326(2) and 2.497(2) Å. Due to weaker trans influence, the Ru-Cl_b bonds trans to terminal chlorides are shorter than the Ru-Cl_b bonds trans to PPh₃ ligands.¹⁶ Thus, the Ru(1)-Cl(3) bond trans to the PPh₃ ligand is relatively longer than all other Ru-C1 lengths. The average Ru(1)-Cl_b and Ru(2)-Cl_b bond lengths respectively 2.411(2) and 2.363(2) Å, strongly suggest the different oxidation states of the Ru(1) and Ru(2) ions of the two asymmetrical octahedral units in **1**•MeOH.

Considering the relatively shorter Ru(2)-Cl_b and Ru(2)-Cl_t (t = terminal) bond lengths, a 3+ state has been assigned to Ru(2) ion. In this respect, the oxidation level of L_{AP}H₂ that exists as L_{AP}²⁺, L_{ISQ}^{•+} and L_{IQ}⁰ forms as given in Chart 2, is significant to analyze. In **1** the C(1)-O(1) and C(6)-N(1) lengths are 1.276(6) and 1.357(6) Å.

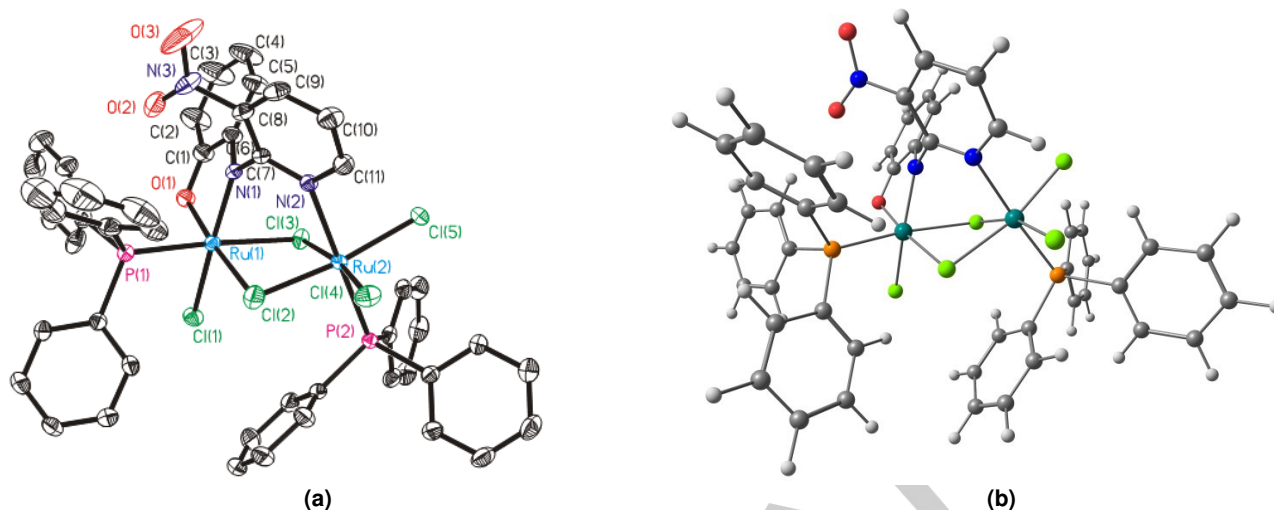


Figure 1. Molecular geometry of (a) **1**·MeOH in crystals (50% thermal ellipsoids, solvent molecules and hydrogen atoms are omitted for clarity) and (b) the gas phase optimized geometry of **1** by hybrid PBE0 DFT method.

(a) $[\text{Ru}^{\text{III}}(\mu\text{-Cl})_3\text{Ru}^{\text{III}}]$				
	Ru1-Cl1	2.398(2)	Ru2-Cl1	2.402(2)
	Ru1-Cl2	2.484(2)	Ru2-Cl2	2.502(2)
	Ru1-Cl3	2.398(2)	Ru2-Cl3	2.392(2)
	Ru1-Cl4	2.321(2)	Ru2-Cl6	2.316(2)
	Ru1-Cl5	2.313(2)	Ru2-Cl7	2.313(2)
	Ru1-Clb (avg)	2.426(2)	Ru2-Clb (avg)	2.432(2)
	(b) $[\text{Ru}^{\text{II}}(\mu\text{-Cl})_3\text{Ru}^{\text{II}}]$			
	Ru1-Cl1	2.46	Ru2-Cl1	2.46
	Ru1-Cl2	2.50	Ru2-Cl2	2.50
	Ru1-Cl3	2.49	Ru2-Cl3	2.52
	Ru1-Clb (avg)	2.48	Ru2-Clb (avg)	2.49
(c) $[\text{Ru}^{\text{II}}(\mu\text{-Cl})_3\text{Ru}^{\text{III}}]$				
	Ru1-Cl1	2.365(2)	Ru2-Cl1	2.351(2)
	Ru1-Cl2	2.476(2)	Ru2-Cl2	2.477(2)
	Ru1-Cl3	2.527(2)	Ru2-Cl3	2.483(2)
	Ru1-Cl4	2.370(2)	Ru2-Cl5	2.357(2)
	Ru1-Clb (avg)	2.456(2)	Ru2-Clb (avg)	2.437(2)
(d) $[\text{Ru}^{\text{II}}(\mu\text{-Cl})_2\text{Ru}^{\text{III}}]$ in 1 ·MeOH				
	Ru1-Cl2	2.326(2)	Ru2-Cl2	2.308(2)
	Ru1-Cl3	2.497(2)	Ru2-Cl3	2.418(2)
	Ru1-Cl1	2.347(2)	Ru2-Cl4	2.311(2)
			Ru2-Cl5	2.329(2)
	Ru1-Clb (avg)	2.411(2)	Ru2-Clb (avg)	2.363(2)

Chart 3. Experimental bond lengths of (a) diruthenium (III, III) unit in $[\text{Ph}_3\text{P}=\text{O} \cdots \cdots \text{H} \cdots \cdots \text{O}=\text{PPh}_3][\text{Ru}_2\text{Cl}_7(\text{PPh}_3)_2] \cdot 0.5(\text{CH}_2\text{Cl}_2)(\text{H}_2\text{O})^{14}$ (b) diruthenium (II, II) unit in $[\text{Ru}_2\text{Cl}_3(\text{PMe}_2\text{Ph})_6]\text{PF}_6^{15}$ (c) diruthenium (II, III) unit in $[\text{Ru}_2\text{Cl}_5(\text{chiraphos})_2]$ (chiraphos = 2(S),3(S)-bis(diphenylphosphino)butane)¹⁶ and (d) **1**·MeOH.

The C-O and C-N lengths of the *o*-iminoquinone forms of a bi-dentate *o*-aminophenol ligand respectively are 1.25 ± 0.01 and 1.30 ± 0.01 Å, while that of the *o*-iminosemiquinonate anion radical are 1.30 ± 0.01 and 1.35 ± 0.01 Å.⁶ However, the C-N lengths of the *o*-iminoquinone and *o*-iminosemiquinonate anion radical forms of a tri-dentate *o*-aminophenol ligand are relatively longer and span the ranges of 1.34 ± 0.01 Å and 1.37 ± 0.01 Å.¹⁷ Considering the trend of the C-N lengths of a tri-dentate *o*-iminoquinone ligand and the C-O length, existence of the L_{IQ}^0 with a minor contribution of L_{ISQ}^{\bullet} states in **1** has been predicted. The C-C lengths of the aminophenol ring of L_{IQ}^0 exhibit quinoidal distortion with shorter C(2)-C(3), 1.340(10) and C(4)-C(5), 1.352(8) Å, lengths. In conjunction with the trend of the Ru-Cl lengths and a major contribution of the L_{IQ}^0 form of the $L_{AP}H_2$ ligand, **1**•MeOH has been defined as a diruthenium (II, III) Robin-Day Class-II complex (where the +2 and +3 oxidation states are assigned to Ru(1) and Ru(2) centres respectively) with a minor contribution of diruthenium (III, III) state containing L_{ISQ}^{\bullet} radical anti-ferromagnetically coupled to the chelated ruthenium (III) ion as shown in Scheme 1.

Metrical oxidation state (MOS) of L_{IQ}^n ($n = 0, -1, -2$) has been calculated by the method introduced by Brown^{2c} using X-ray bond parameters of **1**•MeOH. The calculated MOS is -0.82 that corresponds to the dominant contribution of the L_{IQ}^0 state of the ligand. However the assignment differs significantly as the L_{IQ}^n is a tri-dentate bridging ligand and the metrical parameters of the three redox states of these ligands are quite different¹⁷ from those observed for a bi-dentate ligand.^{2c, 18}

Cyclic Voltammetry. The redox activity of **1** was investigated by cyclic voltammetry at 298 K using tetrabutylammonium hexafluorophosphate or tetrabutylammonium chloride as a supporting electrolyte. The cyclic voltammograms and the redox potential data referenced to the ferrocenium/ferrocene, Fc^+/Fc , couple are given in Figure 2. In CH_2Cl_2 and CH_3CN (10:1) mixture **1** exhibits two reversible cathodic waves at -0.38 and -0.82 V respectively due to $[Ru^{II}(L_{IQ}^0)(\mu-Cl)_2Ru^{III}]/[Ru^{II}(L_{IQ}^0)(\mu-Cl)_2Ru^{II}]$ and $[Ru^{II}(L_{IQ}^0)(\mu-Cl)_2Ru^{III}]/[Ru^{II}(L_{ISQ}^{\bullet})(\mu-Cl)_2Ru^{II}]$ redox couples (Figure 2(a)), however, in this condition no reversible anodic wave was discernible due to the dissociation of the labile PPh_3 ligands. The anodic waves of the voltammogram of **1** recorded in CH_2Cl_2 containing 1.5×10^{-4} M PPh_3 as shown in Figure 2(b) are reversible. In presence of PPh_3 , the cyclic voltammogram of **1** displays anodic waves respectively at +0.52 and +0.85 V, that are assigned to $[Ru^{III}(L_{IQ}^0)(\mu-Cl)_2Ru^{III}]/[Ru^{II}(L_{IQ}^0)(\mu-Cl)_2Ru^{III}]$ and $[Ru^{III}(L_{IQ}^0)(\mu-Cl)_2Ru^{IV}]/[Ru^{III}(L_{IQ}^0)(\mu-Cl)_2Ru^{III}]$ redox couples. To restrict the effect of the chloride dissociation, the cyclic voltammogram of **1** was recorded using tetrabutylammonium chloride as a supporting electrolyte (Figure 2(c)). However, no reversible anodic wave was discernible in this medium too, precluding any effect of the chloride dissociation. In presence of tetrabutylammonium chloride salt, the cathodic waves shift positively by around 100 mV and a new cathodic wave at -0.97 V due to $L_{ISQ}^{\bullet}/L_{AP}^{2-}$ redox couple was detected. The 1^+ , 1^{2+} , 1^{\cdot} and $1^{2\cdot}$ forms were not isolated, but characterized by EPR spectroscopy, NIR absorption bands and BS DFT calculations.

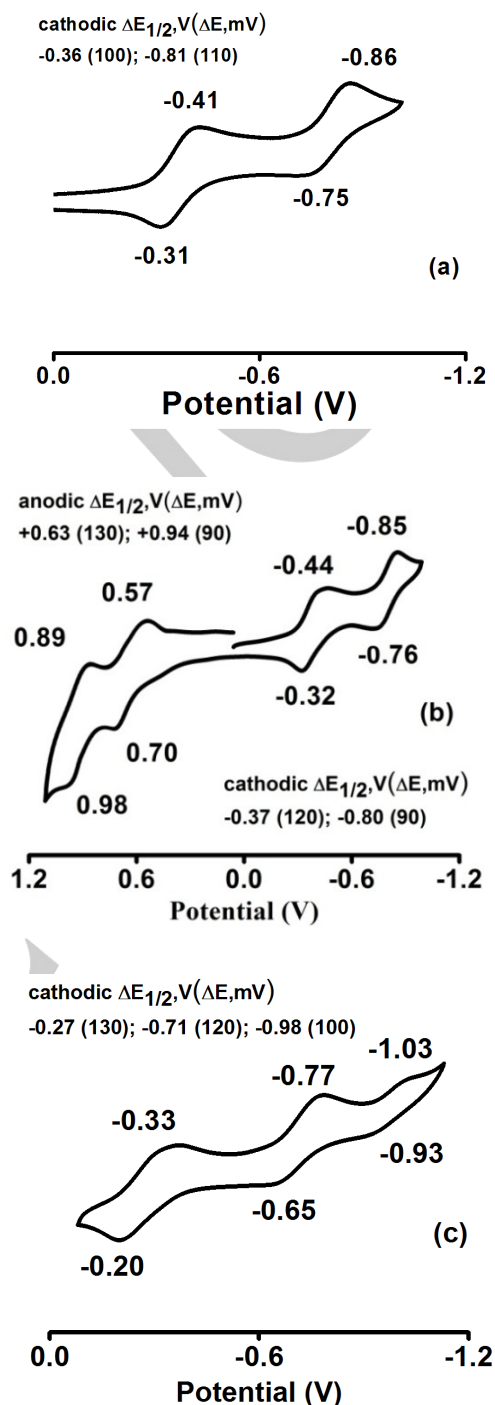


Figure 2. Cyclic voltammograms of **1** in (a) CH_2Cl_2 and CH_3CN (10:1) solvents mixture (b) CH_2Cl_2 containing 1.5×10^{-4} M PPh_3 using 0.2 M $[N(n-Bu)_4]PF_6$ as a supporting electrolyte (c) CH_2Cl_2 containing 0.2 M $[N(n-Bu)_4]Cl$ as a supporting electrolyte at 298 K (potential is referenced to Fc^+/Fc couple).

EPR Spectroscopy. The paramagnetic complexes were also analyzed by EPR spectroscopy. The X-band EPR spectra of the powder sample of **1** and the CH_2Cl_2 solutions of **1**, $1^{2\cdot}$ and 1^{2+} recorded at variable temperatures (298-113 K) are illustrated in

Figure S5. The powder sample of **1** at 113 K exhibits a Ru(2) centre based rhombic spectrum that displays hyperfine splitting due to $^{35,37}\text{Cl}$ nucleus ($I = 3/2$) as illustrated in Figure 3(a). The simulated g and the hyperfine coupling constant (A_{Cl}) are $g_1 = 2.476$, $g_2 = 2.339$ ($A_{\text{Cl}} = 40.0$) and $g_3 = 2.068$ ($A_{\text{Cl}} = 230.0$ MHz) with the anisotropy (Δg), 0.41. The Δg is larger as the RuPNCI₄ octahedron is severely distorted. The frozen glass EPR spectrum of **1** in CH₂Cl₂ at 113 K (Figure 3(b)) is similar to that of the powder sample and the simulated g and A_{Cl} parameters are

$g_1 = 2.481$, $g_2 = 2.360$ ($A_{\text{Cl}} = 125.0$) and $g_3 = 2.049$ ($A_{\text{Cl}} = 190.0$ MHz) with $\Delta g = 0.43$. The similar EPR spectra of the powder and frozen glass confirm that in CH₂Cl₂ **1** is stable. The pattern of the EPR spectra of **1** is similar to those reported for [Ru₃C1₆(PR₃)₆][BPh₄] by Cotton *et al.*¹⁹ Notably, the frozen glass EPR spectrum for the **1**²⁺ ion in CH₂Cl₂ at 113 K is also similar to that of **1**, inferring that the EPR signal of **1**²⁺ ion is also based on the spin centred on Ru(2). The assigned g values for **1**²⁺ ion are $g_1 = 2.484$, $g_2 = 2.391$ and $g_3 = 2.061$ with $\Delta g = 0.42$. The $S = 1/2$ state of Ru(2) of **1**²⁺ ion is achieved by an anti-ferromagnetic coupling interaction between Ru(1)³⁺ (\downarrow) and Ru(2)⁴⁺ ($\uparrow\uparrow$) ions. The EPR spectrum of **1**²⁺ is different from those of the **1** and **1**²⁺. The fluid solution EPR spectrum of **1**²⁺ at 298 K displays a strong signal at $g = 2.008$ due to iminobenzosemiquinonate anion radical and a broader signal at $g = 2.2$ (Figure 4(a)) due to ruthenium (III) ion, while the frozen CH₂Cl₂ glass spectrum of the **1**²⁺ at 113 K is well resolved and exhibits a rhombic EPR signal due to +3 state of Ru(1) ion as given in Figure 4(b). The variable temperature EPR spectra of **1**²⁺ confirming a contribution of ruthenium(III) ion were illustrated in Figure S6. However, no temperature dependent thermal equilibrium between [Ru^{II}(L_{iso}^{*})] and [Ru^{III}(L_{AP}²⁻)] forms was established.

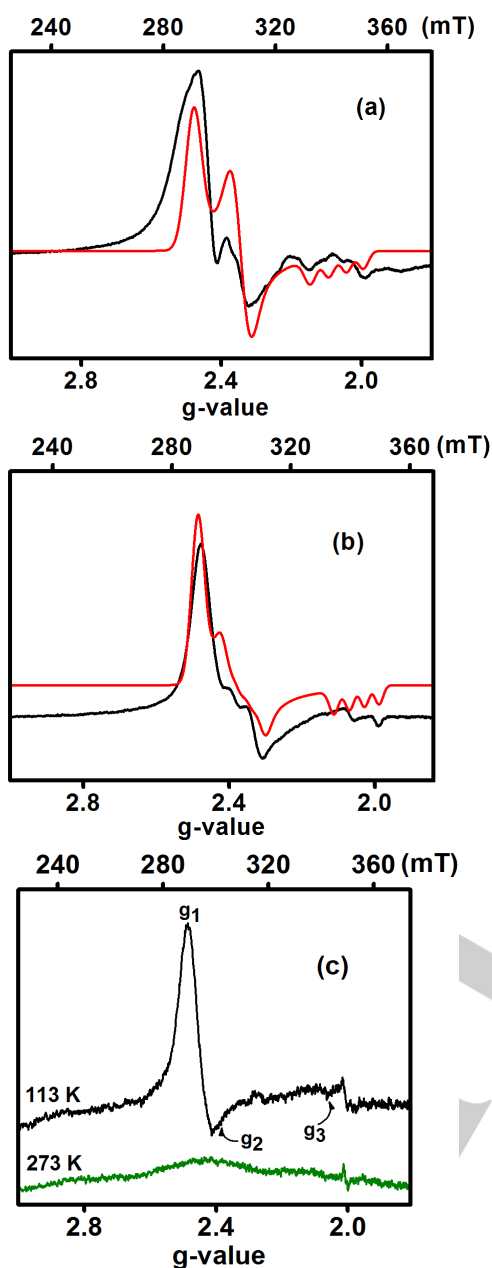


Figure 3. X-band EPR spectra of (a) powder sample of **1** at 113 K (frequency, 9.46827 MHz) (b) frozen CH₂Cl₂ glass of **1** at 113 K (frequency 9.47580 MHz) (experimental, black and simulated, red) and (c) **1**²⁺ ion, fluid solution (in CH₂Cl₂ containing 1.5×10^{-4} M PPh₃) at 273 K (frequency 9.47117 MHz) (green) and frozen glass at 113 K (frequency 9.47667 MHz) (black).

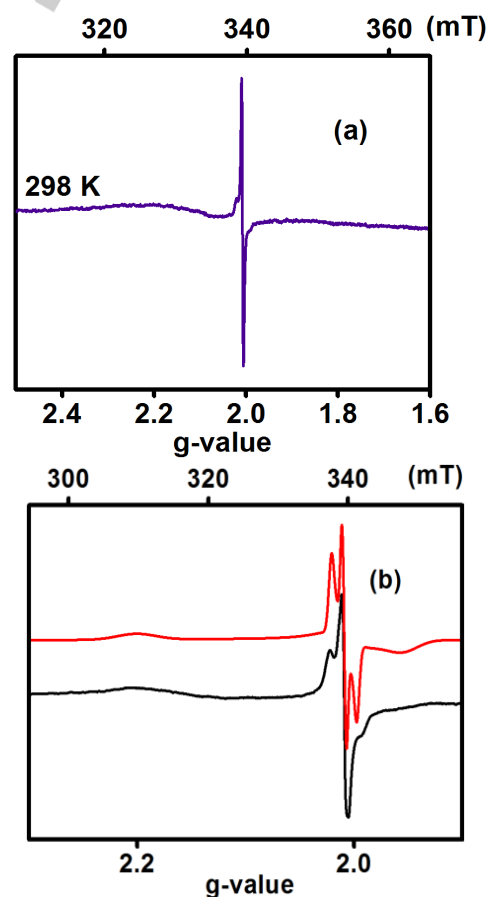
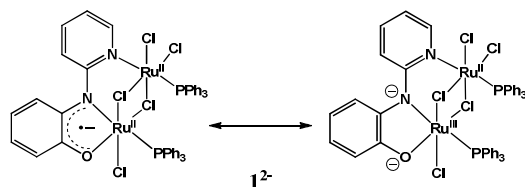
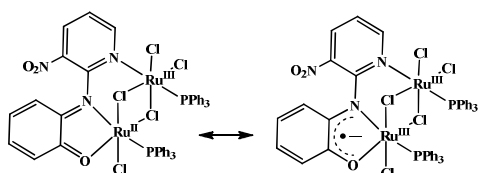


Figure 4. X-band EPR spectra of **1**²⁺, (a) CH₂Cl₂ solution at 298 K (frequency, 9.46130 MHz) and (b) CH₂Cl₂ frozen glass at 113 K (frequency 9.47655 MHz) (experimental, black and simulated, red; simulated spectra was achieved by a combination of two sub-spectra due to [Ru^{II}(L_{AP}²⁻)(μ -Cl)₂Ru^{III}] (33.3%) and [Ru^{II}(L_{iso}^{*})(μ -Cl)₂Ru^{II}] (66.7%) electronic states).

Chart 4. Two electronic states of 1^{2-} Chart 5. $[\text{Ru}^{\text{II}}(\text{L}_{\text{IO}}^0)(\mu\text{-Cl})_2\text{Ru}^{\text{III}}]$ and $[\text{Ru}^{\text{III}}(\text{L}_{\text{ISO}}^{\bullet-})(\mu\text{-Cl})_2\text{Ru}^{\text{II}}]$ forms of 1

The frozen glass spectrum was convoluted into two sub-spectra and simulated considering $[\text{Ru}^{\text{II}}(\text{L}_{\text{AP}}^{2-})(\mu\text{-Cl})_2\text{Ru}^{\text{III}}]$ (33.3%) and $[\text{Ru}^{\text{II}}(\text{L}_{\text{ISO}}^{\bullet-})(\mu\text{-Cl})_2\text{Ru}^{\text{II}}]$ (66.7%) components. The simulated g values for the ruthenium(III) component are $g_1 = 2.201$, $g_2 = 2.005$ and $g_3 = 1.955$, and that for the organic radical component is 2.009.

The two component EPR spectra of the ruthenium(II/III) complexes containing redox noninnocent ligands were reported in several aspects.²⁰ Notably, the frozen glass spectrum due to radical component of 1^{2-} displays hyperfine splitting due to ^{14}N ($I = 1$) nucleus and the simulated hyperfine coupling constant (A_{N}) is 16.5 MHz. The study infers that both $[\text{Ru}^{\text{III}}(\text{L}_{\text{AP}}^{2-})(\mu\text{-Cl})_2\text{Ru}^{\text{II}}]$ and $[\text{Ru}^{\text{II}}(\text{L}_{\text{ISO}}^{\bullet-})(\mu\text{-Cl})_2\text{Ru}^{\text{II}}]$ components coexist in 1^{2-} ion. Expectedly, in fluid solution at 298 K, the spectrum due to ruthenium (III) ion is not resolved. However, the frozen glass reveals a well resolved rhombic spectrum. Thus the ground electronic state of 1^{2-} is defined as a hybrid state of $[\text{Ru}^{\text{II}}(\text{L}_{\text{AP}}^{2-})(\mu\text{-Cl})_2\text{Ru}^{\text{II}}] \leftrightarrow [\text{Ru}^{\text{II}}(\text{L}_{\text{ISO}}^{\bullet-})(\mu\text{-Cl})_2\text{Ru}^{\text{II}}]$ forms as depicted in Chart 4.

Broken Symmetry (BS) DFT Calculations. The electronic structures of 1 and the oxidized and reduced analogues were further confirmed by BS DFT calculations using the ORCA program package.⁶ The gas phase geometry of 1 with a doublet spin state was optimized by the hybrid PBE0 DFT method and the gas phase optimized geometry is shown in Figure 1(b). The calculated bond lengths are summarized in Table 1. For comparison geometry of 1 was also optimized in CH_2Cl_2 and the calculated bond parameters of the gas phase and solution geometries are similar. In 1 , the calculated Ru(1)-Cl(1) length is marginally longer than Ru(2)-Cl(4) and Ru(2)-Ru(5) lengths. The calculated C(1)-O(1) length, 1.283 Å, is an intermediate of that expected for semiquinone (~1.30 Å) and quinone (~1.25 Å) forms. Similarly, the C(6)-N(1) length, 1.350 Å, is relatively longer than that reported for a tri-dentate α -iminoquinone ligand.¹⁸ The calculated spin density obtained from Mulliken spin population analysis scatters on both ruthenium ions and L_{IO}^0 ligand as depicted in Figure 5(a). The trend of the calculated Ru-Cl, C-O and C-N lengths in conjunction with the spin density

distribution predicts the contributions of both $[\text{Ru}^{\text{II}}(\text{L}_{\text{IO}}^0)(\mu\text{-Cl})_2\text{Ru}^{\text{III}}] \leftrightarrow [\text{Ru}^{\text{III}}(\text{L}_{\text{ISO}}^{\bullet-})(\mu\text{-Cl})_2\text{Ru}^{\text{III}}]$ forms (Chart 5) to the ground electronic state of 1 . The quantum chemical result on 1 predicting the nearly equal spin density on both ruthenium ions seems to be a consequence of an over-delocalization.²¹

The gas phase geometry of 1 was optimized with singlet spin state. It is noteworthy that no significant change of the C(1)-O(1) and C(6)-N(1) lengths were observed during the $1 \rightarrow 1^+$ conversion. However, in 1^+ the calculated Ru(1)-Cl(1), 2.387 Å, Ru(2)-Cl(4), 2.389 Å and Ru(2)-Cl(5), 2.393 Å, are significantly longer than those found for 1 . In 1^+ , the Ru(1)-Cl and Ru(2)-Cl terminal and bridging bond lengths (Table 1) are similar and the diruthenium (II, II) state, $[\text{Ru}^{\text{II}}(\text{L}_{\text{IO}}^0)(\mu\text{-Cl})_2\text{Ru}^{\text{II}}]$ has been assigned to 1^+ . The gas phase geometry of 1^{2-} was optimized with a doublet spin state. The calculated lengths for 1^{2-} ion have a different trend. In the transformation of $1^+ \rightarrow 1^{2-}$, the Ru(1)-Cl(1), Ru(2)-Cl(4) and Ru(2)-Cl(5) lengths increase, while Ru(1)-P(1) and Ru(2)-P(2) lengths decrease significantly. It infers that 1^{2-} promotes stronger Ru \rightarrow PPh₃ back-bonding. In 1^{2-} the C(1)-O(1) and C(6)-N(1) lengths respectively are 1.307 and 1.385 Å that are consistent with the $\text{L}_{\text{ISO}}^{\bullet-}$ form of the ligand.¹³ The spin density obtained from the Mulliken spin population analysis is dominantly localized on Ru(1) and the NO-chelate as illustrated in Figure 5(b). Thus contributions of both $[\text{Ru}^{\text{III}}(\text{L}_{\text{AP}}^{2-})(\mu\text{-Cl})_2\text{Ru}^{\text{II}}]$ and $[\text{Ru}^{\text{II}}(\text{L}_{\text{ISO}}^{\bullet-})(\mu\text{-Cl})_2\text{Ru}^{\text{II}}]$ forms to the electronic ground state of 1^{2-} was anticipated. The existence of these two components (Chart 4) to the ground electronic state of 1^{2-} was confirmed by fluid solution and frozen glass EPR spectra (*vide supra*).

The gas phase geometry of 1^+ was optimized with singlet and triplet spin states and these were compared with the broken symmetry (BS) $M_S = 0$ solution. The triplet solution is 81.9 kJ/mol lower in energy than the singlet solution, while the energy of the BS (1,1) solution is similar to that of the triplet solution (only 0.52 kJ/mol higher in energy), inferring the presence of the ruthenium (III, III) state in the 1^+ ion. In the BS state of 1^+ , the calculated Ru(1)-Cl(1), 2.266 Å, Ru(2)-Cl(4), 2.286 Å and Ru(2)-Cl(5), 2.302 Å terminal lengths are comparable and relatively shorter. Notably the Ru(1)-PPh₃, 2.375 Å and Ru(2)-PPh₃, 2.343 Å, lengths increase significantly correlating well with the oxidation of Ru(1)^{II} to Ru(1)^{III}. The C(1)-O(1) and C(6)-N(1) lengths in 1^+ are also relatively shorter than those of 1 . Considering these bond parameters, 1^+ ion has been defined by the $[\text{Ru}^{\text{III}}(\text{L}_{\text{IO}}^0)(\mu\text{-Cl})_2\text{Ru}^{\text{III}}]$ state.

The gas phase geometry of 1^{2+} was optimized with doublet and quartet spin states. The energy of the BS $M_S = 1/2$ of 1^{2+} was calculated by a flip spin method. Notably, the energy of the high spin quartet solution is 26.9 kJ/mol lower than the doublet solution, while the BS (III, IV) $M_S = 1/2$ solution is 0.71 kJ/mol lower in energy than that of high spin quartet solution. Thus, 1^{2+} ion is described by a $[\text{Ru}^{\text{III}}(\text{L}_{\text{IO}}^0)(\mu\text{-Cl})_2\text{Ru}^{\text{IV}}]$ state. In $1^+ \rightarrow 1^{2+}$ transformation, the Ru(1)-Cl(1) length decreases to 2.252 Å, while the Ru(1)-PPh₃ length changes to 2.367 Å. The Ru(2)-Cl(4) and Ru(2)-Cl(5) lengths respectively are 2.255 and 2.240 Å which are distinctly shorter than those of the 1^+ ion. The calculated lengths are also shorter than those reported for ruthenium (IV) complexes.²² In 1^{2+} , the C(1)-O(1) and C(6)-N(1) lengths, 1.264 and 1.333 Å, are shorter and have been

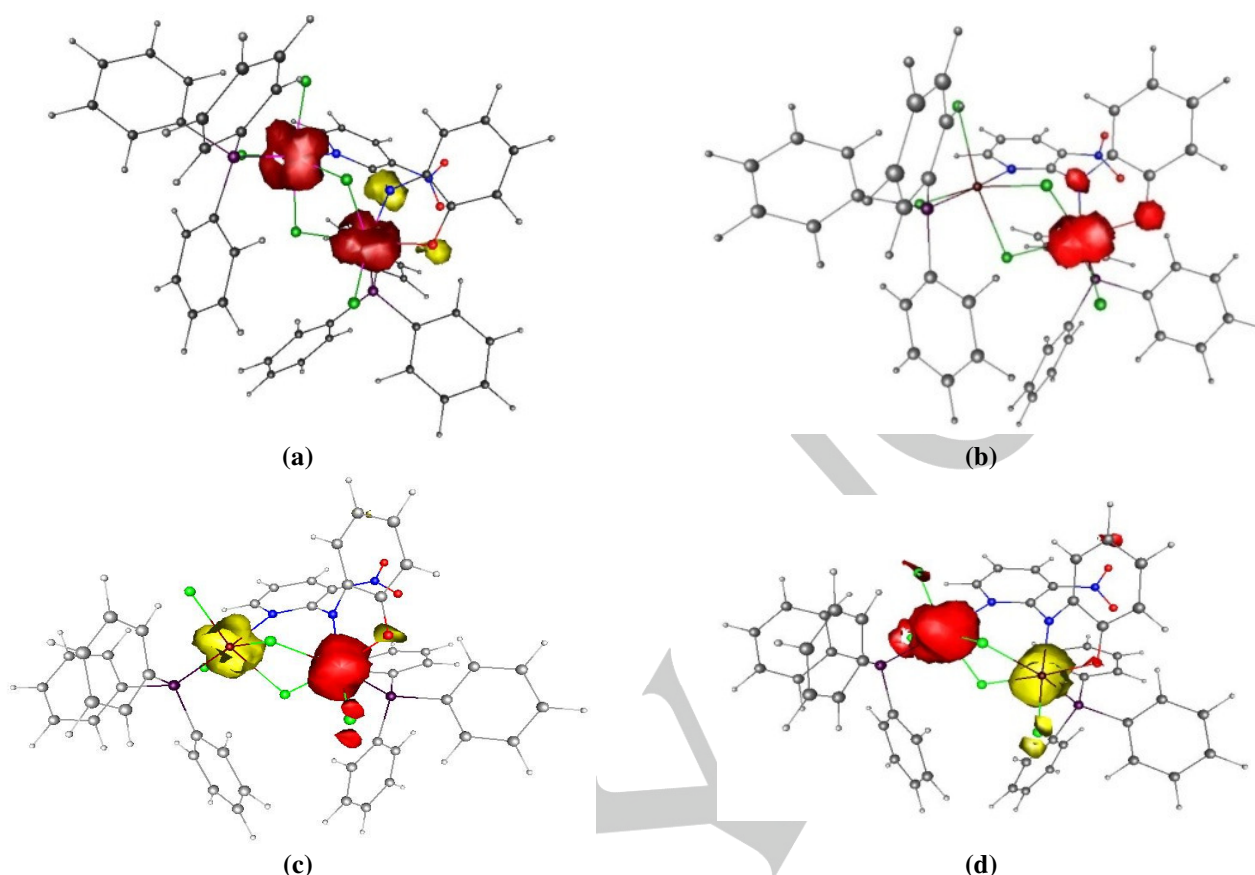


Figure 5. Mulliken spin density plots with isovalue 0.01 obtained from unrestricted DFT calculations on (a) **1** [PBE0, Ru(1), 0.65; Ru(2), 0.88; O(1), -0.10; N(1), -0.25; C(1), -0.13; C(2), 0.04; C(3), -0.10; C(4), -0.06; C(6), -0.07; Cl(1), 0.05; Cl(4), 0.06; Cl(5), 0.07] and (b) 1^{2-} [Ru(1), 0.63; Ru(2), 0.02; O(1), 0.12; N(1), 0.07; C(2), 0.04; C(4), 0.03]. Spin density plot obtained from broken symmetry DFT calculations on (c) 1^+ [Ru(1), 1.05; Cl(1), 0.19; Cl(2), +0.07; Ru(2), -0.85; Cl(4), -0.08; Cl(5), -0.08; Cl(3), -0.04; C(1), -0.07; C(4), -0.09; C(5), 0.06; C(6), -0.11] and (d) 1^{2+} [Ru(1), -1.08; Cl(1), -0.20; Ru(2), +1.59; Cl(4), +0.24; Cl(5), +0.14; C(4), +0.11; O(1), +0.04] (red, alpha spin; yellow, beta spin).

considered as the markers for the L_{IQ} state of $L_{AP}H_2$ in this dinuclear core. The spin density obtained from Mulliken spin population analysis is dominantly localized on Ru(1), -1.08 (beta spin) and Ru(2), +1.59 (alpha spin) centres as shown in Figure 5(d) and is consistent with the dinuclear ruthenium (III, IV) state of 1^{2+} ion.

UV-Vis-NIR Absorption Spectra. The UV-Vis-NIR absorption spectra of $L_{AP}H_2$, **1** and 1^+ , 1^{2+} , 1^- and 1^{2-} obtained from constant potential bulk electrolysis experiments in CH_2Cl_2 at 298K were recorded and are illustrated in Figure 6. $L_{AP}H_2$ exhibits strong absorption bands at 425 and 290 nm. The absorption spectrum of **1** displays a NIR band at 1300 nm (Figure 6(b)) due to a $Ru^{II} \rightarrow Ru^{III}$ intervalence charge transfer (IVCT) transition. Similarly, the 1^{2+} ion exhibits a $Ru^{III} \rightarrow Ru^{IV}$ IVCT transition at 1370 nm. The IVCT transitions correlate with the Robin-Day class II electronic states of **1** and 1^{2+} ion. Notably, the lower energy band is absent in the 1^+ and 1^- ions containing (Ru^{III} , Ru^{III}) and (Ru^{II} , Ru^{II}) cores. The 1^{2-} ion exhibits a broader absorption band at 1000 nm.

Table 2. UV-Vis-NIR Absorption Spectral Data of $L_{AP}H_2$, **1**, 1^+ , 1^{2+} , 1^- and 1^{2-} in CH_2Cl_2

Compounds	λ_{max} , nm (ϵ , $10^3 M^{-1}cm^{-1}$)
$L_{AP}H_2$	425 (3.23), 290 (7.19)
1	1300 (0.14), 560 (1.40), 500 (1.30), 360 (1.67)
1^+	560 (0.88), 375 (1.11)
1^{2+}	1370 (0.17), 550 (1.42), 425 (1.75)
1^-	570 (1.16), 380 (2.00)
1^{2-}	540 (0.50), 375 (0.88)

^a containing 1.5×10^{-4} M PPh_3

All these dinuclear complexes exhibit a stronger absorption band at 540-560 nm (Figure 7) which are ubiquitous for Ru^{II} -quinone complexes.^{17, 20} The origin of the transition was elucidated by TD

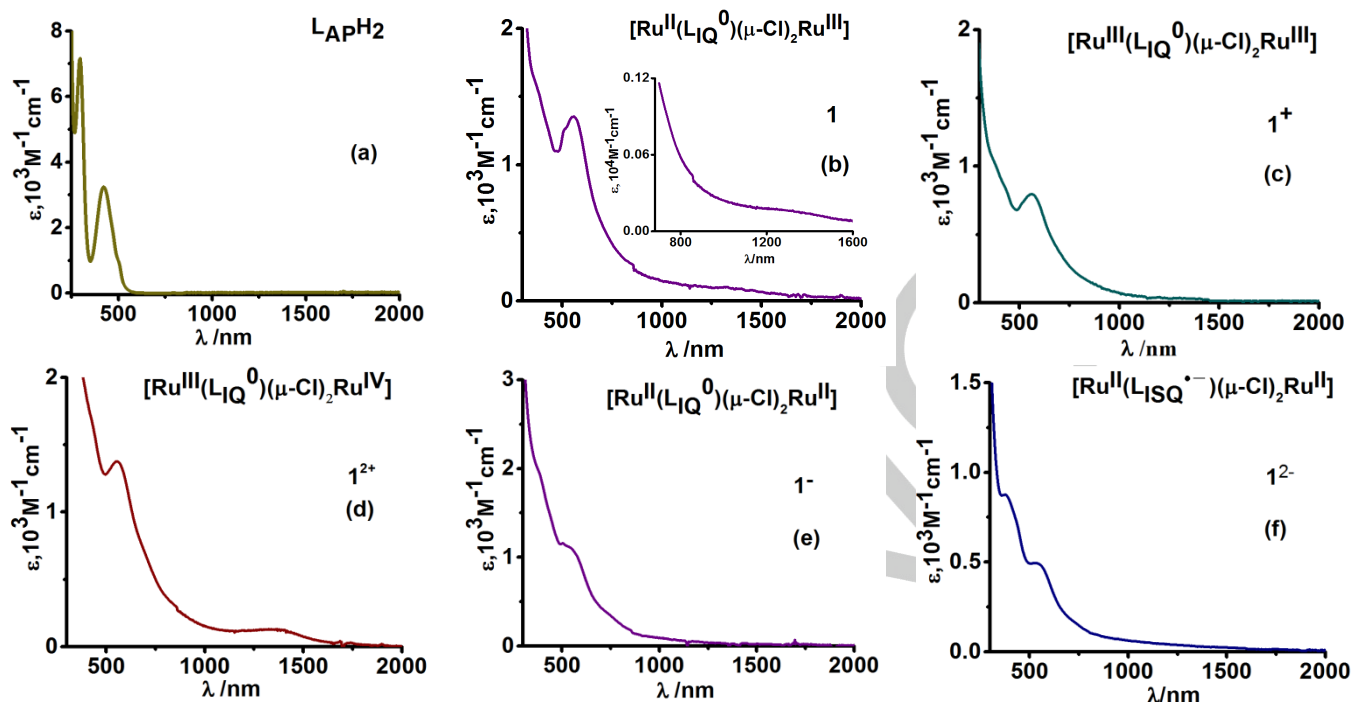


Figure 6. UV-Vis-NIR absorption spectra of $L_{AP}H_2$, 1 , 1^- and 1^{2-} in CH_2Cl_2 and 1^+ , 1^{2+} in CH_2Cl_2 containing 1.5×10^{-4} M PPh_3 .

DFT calculation on 1 in CH_2Cl_2 . The calculated wave lengths are listed in Table 3. The DFT calculation confirms that the absorption band at 500-600 nm is due to the metal to ligand charge transfer (MLCT) and metal to mixed metal-ligand charge transfer (MMMLCT) transitions. Notably, this MLCT transition is significantly perturbed during $1 \rightarrow 1^+$ and $1 \rightarrow 1^-$ conversions. The changes of UV-vis absorption pattern during $1 \rightarrow 1^+$, $1 \rightarrow 1^{2+}$, $1 \rightarrow 1^-$ and $1^- \rightarrow 1^{2-}$ conversions were recorded by spectroelectrochemical measurements (Figure 7) in CH_2Cl_2 . It was recorded that in $1 \rightarrow 1^-$ conversion, where $[Ru^{II}(L_{IQ}^0)(\mu-Cl)_2Ru^{III}]$ is reduced to $[Ru^{II}(L_{IQ}^0)(\mu-Cl)_2Ru^{II}]$ state, the MLCT band at 560 nm gradually diminishes and a broader band at 750 nm appears showing two isosbestic points at 650 and 480 nm. In the $1^- \rightarrow 1^{2-}$ conversion due to the reduction of iminobenzoquinone to iminobenzosemiquinonate anion radical the MLCT transition gradually diminishes and the spectrum changes showing one isosbestic point at 390 nm. In $1 \rightarrow 1^+$ conversion, where $[Ru^{II}(L_{IQ}^0)(\mu-Cl)_2Ru^{III}]$ is oxidised to $[Ru^{III}(L_{IQ}^0)(\mu-Cl)_2Ru^{III}]$ state, the MLCT band changes showing two isosbestic points at 515 and 660 nm. However, during $1^+ \rightarrow 1^{2+}$ conversion, the major bands disappear generating a peak at 550 nm.

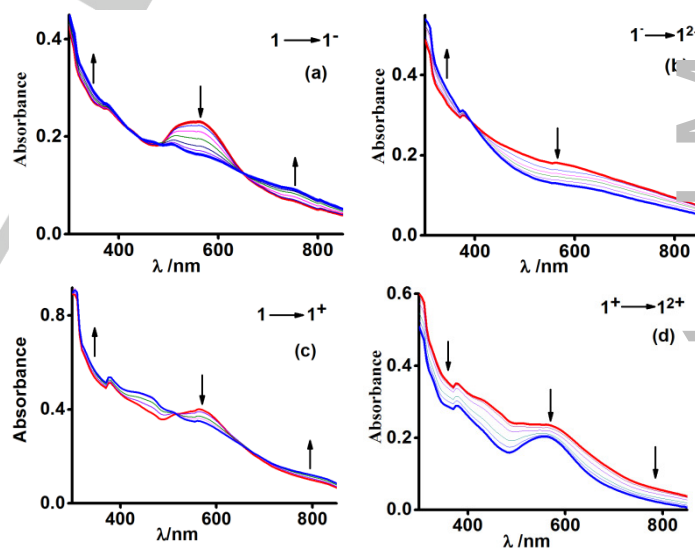


Figure 7. Change of absorption spectra during (a) $1 \rightarrow 1^-$ (CH_2Cl_2) (b) $1^- \rightarrow 1^{2-}$ (CH_2Cl_2) and (c) $1 \rightarrow 1^+$ (CH_2Cl_2 containing 1.5×10^{-4} M PPh_3) and (d) $1^+ \rightarrow 1^{2+}$ (CH_2Cl_2 containing 1.5×10^{-4} M PPh_3) conversions achieved by constant potential spectroelectrochemical measurements at 298 K (initial spectrum, red and final spectrum, dark blue).

Table 3. Calculated Excitation Energies (λ_{nm}), Oscillator Strengths (f) and Transition Types Obtained from TD DFT Calculation on **1** in CH_2Cl_2 using PBE0 hybrid functional

λ_{cal}	f	λ_{exp}	Significant Transitions (>10%)	Transitions Types
597.6	0.014	560	α -HOMO-3 \rightarrow LUMO (18%) β -HOMO-3 \rightarrow LUMO (12%) β -HOMO-1 \rightarrow LUMO (12%)	$d_{\text{Ru}} \rightarrow \pi^*$ (MLCT) $d_{\text{Ru}} \rightarrow \pi^*+d_{\text{Ru}}$ (MMMLCT) $d_{\text{Ru}}+p_{\text{Cl}} \rightarrow \pi^*+d_{\text{Ru}}$ (MMMLCT)
490.7	0.068	500	α -HOMO-5 \rightarrow LUMO (28%)	$\text{PPh}_3 \rightarrow \pi^*$ (LLCT)

MLCT = metal to ligand charge transfer; MMMLCT = metal to mixed metal-ligand charge transfer; LLCT = ligand to ligand charge transfer.

Conclusions

Coordination of redox noninnocent ligands to transition metal ions is common for natural electron transfer proteins those undergo with various mixed-valence states. In this study, it is disclosed that a combination of redox non-innocent and innocent donor sites in a ligand is significant in modelling mixed valence complexes of transition metal ions. In this context, a N-pyridyl-*o*-aminophenol derivative containing a redox non-innocent NO- and a redox innocent pyridine nitrogen donor sites, abbreviated as ($\text{L}_{\text{AP}}\text{H}_2$) and a mixed valence diruthenium (II, III) complex, $[(\text{PPh}_3)_2\text{Cl}_2\text{Ru}^{\text{II}}(\text{L}_{\text{IQ}}^0)(\mu\text{-Cl})_2\text{Ru}^{\text{III}}\text{Cl}(\text{PPh}_3)]$ (**1**) were successfully isolated (L_{IQ}^0 is the 2e oxidized *o*-iminobenzoquinone form of $\text{L}_{\text{AP}}\text{H}_2$). $1/1^+$ and $1^+/1^{2+}$ redox couples are reversible, while $1^+/1$ and $1^{2+}/1^+$ redox couples are not due to PPh_3 dissociation, however they are reversible in CH_2Cl_2 containing 1.5×10^{-4} M PPh_3 solution. Single crystal X-ray crystallography, EPR spectroscopy, spectroelectrochemical measurement, inter valence charge transfer (IVCT) transition and broken symmetry (BS) DFT calculations confirm that **1** and 1^{2+} are respectively diruthenium (II, III), $[\text{Ru}^{\text{II}}(\text{L}_{\text{IQ}}^0)(\mu\text{-Cl})_2\text{Ru}^{\text{III}}]$ and diruthenium (III, IV), $[\text{Ru}^{\text{III}}(\text{L}_{\text{IQ}}^0)(\mu\text{-Cl})_2\text{Ru}^{\text{IV}}]$, mixed valence complexes, while 1^+ and 1 are diruthenium (III, III), $[\text{Ru}^{\text{III}}(\text{L}_{\text{IQ}}^0)(\mu\text{-Cl})_2\text{Ru}^{\text{III}}]$ and diruthenium (II, II), $[\text{Ru}^{\text{II}}(\text{L}_{\text{IQ}}^0)(\mu\text{-Cl})_2\text{Ru}^{\text{II}}]$ complexes of (L_{IQ}^0). The ground electronic state of 1^{2+} is analyzed by a hybrid state of $[\text{Ru}^{\text{II}}(\text{L}_{\text{ISQ}}^{\bullet})(\mu\text{-Cl})_2\text{Ru}^{\text{II}}] \leftrightarrow [\text{Ru}^{\text{III}}(\text{L}_{\text{AP}}^{2-})(\mu\text{-Cl})_2\text{Ru}^{\text{II}}]$ forms. The NIR absorption spectra of 1^+ and 1^{2+} display IVCT transition at 1300 and 1370 nm, while the IVCT bands are absent in other analogues. The study ushers that a combination of redox innocent and redox noninnocent donor sites in a ligand is worthy in stabilizing different redox states of a metal ion in the dinuclear and polynuclear forms and makes the theme of isolating mixed valence complexes of a transition metal ion successful.

Acknowledgements

The authors acknowledge the financial support received from DST (EMR/2016/005222). DD is an INSPIRE fellow of DST (IF131158), New Delhi, India.

Keywords: • di-ruthenium mixed valence complex • organic radical • IVCT transition • broken symmetry DFT • asymmetric bridging ligand.

References

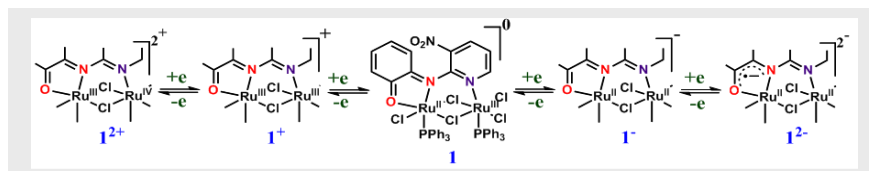
- [1] a) M. Parthey, J. B. G. Gluyas, M. A. Fox, P. J. Low, M. Kaupp, *Chem. Eur. J.* **2014**, *20*, 6895-6908. b) A. Heckmann, L. Christoph, *Angew. Chem. Int. Ed.* **2012**, *51*, 326-392. c) B. Sarkar, S. Patra, J. Fiedler, R. B. Sunoj, D. Janardanan, G. K. Lahiri, W. Kaim, *J. Am. Chem. Soc.* **2008**, *130*, 3532-3542. d) R. C. Rocha, F. N. Rein, H. Jude, A. P. Shreve, J. J. Concepcion, T. J. Meyer, *Angew. Chem.* **2008**, *120*, 513-516. e) K. D. Demadis, C. M. Hartshorn, T. J. Meyer, *Chem. Rev.* **2001**, *101*, 2655-2685.
- [2] Ligand Mixed Valency: a) S. D. J. McKinnon, B. O. Patrick, A. B. P. Lever, R. G. Hicks, *Inorg. Chem.* **2013**, *52*, 8053-8066. b) C. P. Kubiak, *Inorg. Chem.* **2013**, *52*, 5663-5676. c) S. N. Brown, *Inorg. Chem.* **2012**, *51*, 1251-1260. d) C. G. Pierpont, *Inorg. Chem.* **2011**, *50*, 9766-9772. e) A. Das, T. Scherer, S. T. K. Maji, S. M. Mobin, F. A. Urbanos, R. Jimenez-Aparicio, W. Kaim, G. K. Lahiri, *Inorg. Chem.* **2011**, *50*, 7040-7049. f) T. J. Mooibroek, G. Aromí, M. Quesada, O. Roubeau, P. Gamez, S. DeBeer George, J. van Slageren, S. Yasin, E. Ruiz, J. Reedijk, *Inorg. Chem.* **2009**, *48*, 10643-10651. g) P. H. Dinolfo, S. J. Lee, V. Coropceanu, J. L. Brédas, J. T. Hupp, *Inorg. Chem.* **2005**, *44*, 5789-5797. h) A. P. Meacham, K. L. Druce, Z. R. Bell, M. D. Ward, J. B. Keister, A. B. P. Lever, *Inorg. Chem.* **2003**, *42*, 7887-7896. i) H. C. Chang, K. Mochizuki, S. Kitagawa, *Inorg. Chem.* **2002**, *41*, 4444-4452.
- [3] a) E. I. Solomon, X. Xie, A. Dey, *Chem. Soc. Rev.* **2008**, *37*, 623-638. b) J. Stubbe, W. A. van der Donk, *Chem. Rev.* **1998**, *98*, 705-762.
- [4] Creutz and Taube Complex: a) C. Creutz, H. Taube, *J. Am. Chem. Soc.* **1973**, *95*, 1086-1094. b) C. Creutz, H. Taube, *J. Am. Chem. Soc.* **1969**, *91*, 3988-3989.
- [5] a) F. F. Khan, J. Klein, J. L. Priego, B. Sarkar, R. J. Aparicio, G. K. Lahiri, *Inorg. Chem.*, **2018**, *57*, 12800-12810. b) A. Mandal, A. Grupp, B. Schwederski, W. Kaim, G. K. Lahiri, *Inorg. Chem.* **2015**, *54*, 10049-10057. c) A. Mandal, H. Agarwala, R. Ray, S. Plebst, S. M. Mobin, J. L. Priego, R. J. Aparicio, W. Kaim, G. K. Lahiri, *Inorg. Chem.* **2014**, *53*, 6082-6093. d) A. K. Das, B. Sarkar, J. Fiedler, S. Zális, I. Hartenbach, S. Strobel, G. K. Lahiri, W. Kaim, *J. Am. Chem. Soc.* **2009**, *131*, 8895-8902. e) S. Maji, B. Sarkar, S. M. Mobin, J. Fiedler, F. A. Urbanos, R. J. Aparicio, W. Kaim, G. K. Lahiri, *Inorg. Chem.* **2008**, *47*, 5204-5211. f) B. Sarkar, S. Patra, J. Fiedler, R. B. Sunoj, D. Janardanan, G. K. Lahiri, W. Kaim, *J. Am. Chem. Soc.* **2008**, *130*, 3532-3542. g) M. Koley, B. Sarkar, S. Ghumaan, E. Bulak, J. Fiedler, W. Kaim, G. K. Lahiri, *Inorg. Chem.*, **2007**, *46*, 3736-3742. h) M. Koley, B. Sarkar, S. Ghumaan, E. Bulak, J. Fiedler, W. Kaim, G. K. Lahiri, *Inorg. Chem.* **2007**, *46*, 3736-3742. i) S. Ghumaan, S. Kar, S. M. Mobin, B. Harish, V. G. Puranik, G. K. Lahiri, *Inorg. Chem.* **2006**, *45*, 2413-2423. j) S. Patra, B. Sarkar, S. Ghumaan, J. Fiedler, W. Kaim, G. K. Lahiri, *Inorg. Chem.* **2004**, *43*, 6108-6113. k) N. Chanda, B. Sarkar, S. Kar, J. Fiedler, W. Kaim, G. K. Lahiri, *Inorg. Chem.* **2004**, *43*, 5128-5133. l) S. Kar, N. Chanda, S. M. Mobin, A. Datta, F. A. Urbanos, V. G. Puranik, R. Jimenez-Aparicio, G. K. Lahiri, *Inorg. Chem.* **2004**, *43*, 4911-4920. m) S. Patra, T. A. Miller, B.

- Sarkar, M. Niemeyer, M. D. Ward, G. K. Lahiri, *Inorg. Chem.* **2003**, *42*, 4707-4713. n) S. Patra, B. Mondal, B. Sarkar, M. Niemeyer, G. K. Lahiri, *Inorg. Chem.* **2003**, *42*, 1322-1327.
- [6] a) P. Sarkar, M. K. Mondal, A. Sarmah, S. Maity, C. Mukherjee, *Inorg. Chem.* **2017**, *56*, 8068-8077. b) R. Rakshit, S. Ghorai, S. Biswas, C. Mukherjee, *Inorg. Chem.* **2014**, *53*, 3333-3337. c) S. Kundu, S. Maity, A. N. Maity, S.-C. Ke, P. Ghosh, *Dalton Trans.* **2013**, *42*, 4586-4601. d) A. S. Roy, P. Saha, N. D. Adhikary, P. Ghosh, *Inorg. Chem.* **2011**, *50*, 2488-2500. e) C. Mukherjee, T. Weyhermüller, E. Bothe, P. Chaudhuri, *Inorg. Chem.* **2008**, *47*, 2740-2746. f) S. Kokatam, T. Weyhermüller, E. Bothe, P. Chaudhuri, K. Wieghardt, *Inorg. Chem.* **2005**, *44*, 3709-3717.
- [7] a) G. M. Sheldrick, *Acta Crystallogr. Sect. C: Struct. Chem.* **2015**, *71*, 3-8. b) G. M. Sheldrick, *Acta Cryst.* **2008**, *A64*, 112-122.
- [8] F. Neese, *Wiley Interdiscip. Rev.: Comput. Mol. Sci.* **2012**, *2*, 73-78.
- [9] a) A. D. Becke, *J. Chem. Phys.* **1993**, *98*, 5648-5652. b) B. Miehlich, A. Savin, H. Stoll, H. Preuss, *Chem. Phys. Lett.* **1989**, *157*, 200-206. c) C. Lee, W. Yang, R. G. Parr, *Phys. Rev. B* **1988**, *37*, 785-789.
- [10] F. Neese, *J. Phys. Chem. Solids* **2004**, *65*, 781-785.
- [11] a) F. Weigend, R. Ahlrichs, *Phys. Chem. Chem. Phys.* **2005**, *7*, 3297-3305. b) F. Weigend, F. Furche, R. Ahlrichs, *J. Chem. Phys.* **2003**, *119*(24), 12753-12762. c) K. Eichkorn, F. Weigend, O. Treutler, R. Ahlrichs, *Theor. Chem. Acc.* **1997**, *97*, 119-124. d) A. Schaefer, C. Huber, R. Ahlrichs, *J. Chem. Phys.* **1994**, *100*, 5829-5835. e) A. Schaefer, H. Horn, R. Ahlrichs, *J. Chem. Phys.* **1992**, *97*, 2571-2577.
- [12] a) S. Kossmann, F. Neese, *J. Chem. Theory Comput.* **2010**, *6*, 2325-2338. b) H. B. Schlegel, J. J. McDouall, *In Computational Advances in Organic Chemistry*. C. Ogretir, I. G. Csizmadia, Eds. Kluwer Academic: The Netherlands, 1991.
- [13] a) R. E. Stratmann, G. E. Scuseria, M. Frisch, *J. Chem. Phys.* **1998**, *109*, 8218-8224. b) M. E. Casida, C. Jamoroski, K. C. Casida, D. R. Salahub, *J. Chem. Phys.* **1998**, *108*, 4439-4449. c) R. Bauernschmitt, M. Haser, O. Treutler, R. Ahlrichs, *Chem. Phys. Lett.* **1996**, *256*, 454-464. d) M. Cossi, N. Rega, G. Scalmani, V. Barone, *J. Comput. Chem.* **2003**, *24*, 669-681. e) V. Barone, M. Cossi, *J. Phys. Chem. A* **1998**, *102*, 1995-2001.
- [14] M. P. de Araujo, *Transition Metal Chem.* **2002**, *27*, 110-114.
- [15] M. Laing, L. Pope, *Acta Cryst.* **1976**, *B32*, 1547.
- [16] I. S. Thorburn, S. J. Rettig, B. R. James, *Inorg. Chem.* **1986**, *25*, 234-240.
- [17] a) S. Maity, S. Kundu, S. Mondal, S. Bera, P. Ghosh, *Inorg. Chem.* **2017**, *56*, 3363-3376. b) S. Maity, S. Kundu, S. Bera, T. Weyhermüller, P. Ghosh, *Eur. J. Inorg. Chem.* **2016**, 3691-3697. c) S. Bera, S. Mondal, S. Maity, T. Weyhermüller, P. Ghosh, *Inorg. Chem.* **2016**, *55*, 4746-4756. d) M. Bubrin, D. Schweinfurth, F. Ehret, S. Zálíš, H. Kvapilová, J. Fiedler, Q. Zeng, F. Hartl, W. Kaim, *Organometallics* **2014**, *33*, 4973-4985. e) R. Hübner, S. Weber, S. Strobel, B. Sarkar, S. Zálíš, W. Kaim, *Organometallics* **2011**, *30*, 1414-1418.
- [18] S. Kundu, S. Maity, T. Weyhermüller, P. Ghosh, *Inorg. Chem.* **2013**, *52*, 7417-7430.
- [19] F. A. Cotton, R. C. Torralba, *Inorg. Chem.* **1991**, *30*, 4386-4391.
- [20] a) S. Kundu, D. Dutta, S. Maity, T. Weyhermüller, P. Ghosh, *Inorg. Chem.*, **2018**, *57*, 11948-11960. b) M. K. Biswas, S. C. Patra, A. N. Maity, S.-C. Ke, N. D. Adhikary, P. Ghosh, *Inorg. Chem.* **2012**, *51*, 6687-6699.
- [21] M. Parthey, M. Kaupp, *Chem. Soc. Rev.* **2014**, *43*, 5067-5088.
- [22] J. Díez, J. Gimeno, I. Merino, E. Rubio, F. J. Suarez, *Inorg. Chem.* **2011**, *50*, 4868-4881.

Entry for the Table of Contents (Please choose one layout)

Layout 2:

FULL PAPER



Debarpan Dutta,^[a] Suman Kundu^[a] and
Prasanta Ghosh^{*[a]}

Page No. – Page No.

A Di-ruthenium Complex of a N-Pyridyl-o-Aminophenol Derivative: A Route to Mixed Valency

Mixed valence di-ruthenium complexes of 2-((3-nitropyridin-2-yl)amino)phenol containing redox innocent and non-innocent coordination sites are disclosed.